RSC Advances

PAPER

View Article Online
View Journal | View Issue

Check for updates

Cite this: *RSC Adv.*, 2019, **9**, 29590

Acridine-based thiosemicarbazones as novel inhibitors of mild steel corrosion in 1 M HCl: synthesis, electrochemical, DFT and Monte Carlo simulation studies

Ekemini D. Akpan, [ab] Ibanga O. Isaac,[c] Lukman O. Olasunkanmi, [abd]
Eno E. Ebenso *[ab] and El-Sayed M. Sherif [ef]

Received 25th June 2019
Accepted 13th September 2019

DOI: 10.1039/c9ra04778f

rsc.li/rsc-advances

Electrochemical, surface morphology, density functional theory and Monte Carlo simulation methods were employed in investigating the effects of (2*E*,2′*E*)-2,2′-(3,3,6,6-tetramethyl-9-phenyl-3,4,6,7-tetrahydroacridine-1,8(2*H*,5*H*,9*H*,10*H*)-diylidene)bis(*N*-phenylhydrazinecarbothioamide) (IAB-NP), (2*E*,2′*E*)-2,2′-(3,3,6,6-tetramethyl-9-phenyl-3,4,6,7-tetrahydroacridine-1,8(2*H*,5*H*,9*H*,10*H*)-diylidene)bis(*N*-(2,4-difluorophenyl)hydrazinecarbothioamide)IAB-ND) and (2*E*,2′*E*)-2,2′-(3,3,6,6-tetramethyl-9-phenyl-3,4,6,7-tetrahydroacridine-1,8(2*H*,5*H*,9*H*,10*H*)-diylidene)bis(*N*-(2-fluorophenyl) hydrazinecarbothioamide) (IAB-NF) on mild steel corrosion in 1 M HCl solution. From the studies, compounds IAB-NP, IAB-ND and IAB-NF inhibit mild steel corrosion in the acid and the protection efficiencies were found to increase with the increase in concentration of each compound. At the optimum inhibitor concentration of 1.5×10^{-4} M, the inhibition efficiencies (%) of the compounds are in the order IAB-NF (90.48) > IAB-ND (87.48) > IAB-NP (85.28). Potentiodynamic polarization measurements revealed that all the compounds acted as mixed-type corrosion inhibitors. Experimental data for the adsorption of the studied molecules on a mild steel surface in 1 M HCl fitted into the Langmuir adsorption isotherm and the standard free energies of adsorption ($\Delta G^{\circ}_{\text{ads}}$) suggested both physisorption and chemisorption mechanisms. Scanning electron microscopy analyses confirmed the formation of a protective film on the mild steel surface by the inhibitor molecules, resulting in protection of the metal from corrosive electrolyte ions. The experimental findings were corroborated by both theoretical density functional theory and Monte Carlo simulation studies.

Introduction

There is a continuous increase in the use of mild steel in the construction and chemical industries and also for domestic appliances because mild steel is relatively cheap and possesses advantageous mechanical properties.[1] Exposure of mild steel to aqueous environments, especially concentrated acidic environments results in the electro-dissolution and corrosion of the metal.[2,3] Susceptibility of metals to corrosion in nearly all industrial environments has limited the advancement of new technologies.[4] Increasing the durability of construction materials and essential infrastructures such as rail tracks, bridges and metallic structures including cars, storage tanks, corrugated iron, *etc.* by decreasing the rate of corrosion becomes necessary. Because of wide applicability, high efficiency and other numerous advantages, the use of inhibitors stands out as the most efficient method in mitigating corrosion.[5,6]

Currently, there is a growing and continuous need to develop active, appropriate and environmentally friendly inhibitors to mitigate the electro-dissolution and corrosion of metals.[7] Mostly studied and widely utilized corrosion inhibitors are compounds containing heteroatoms, such as nitrogen, sulphur, oxygen and π-electron systems. Moreover, previous studies have revealed that these organic compounds inhibit corrosion by adsorption on the surface of the metal.[4,7–9] Organic molecules used as corrosion inhibitors protect the metals from the corrosive species in the immediate environment by forming resistive layer on the metal surface, which ensures high resistance to electron transfer reactions.[10,11] Molecular orbitals and

---

[a] Department of Chemistry, Faculty of Natural and Agricultural Sciences, North-West University, Private Bag X2046, Mmabatho 2735, South Africa. E-mail: Eno.Ebenso@nwu.ac.za

[b] Material Science Innovation & Modelling (MaSIM) Research Focus Area, Faculty of Natural and Agricultural Sciences, North-West University, Private Bag X2046, Mmabatho 2735, South Africa

[c] Department of Chemistry, Faculty of Natural and Applied Sciences, Akwa Ibom State University, Ikot Akpaden, Akwa Ibom State, Nigeria

[d] Department of Chemistry, Faculty of Science, Obafemi Awolowo University, Ile-Ife 220005, Nigeria

[e] Center of Excellence for Research in Engineering Materials (CEREM), King Saud University, P. O. Box 800, Al-Riyadh 11421, Saudi Arabia

[f] Electrochemistry and Corrosion Laboratory, Department of Physical Chemistry, National Research Centre, El-Behoth St. 33, Dokki, Cairo 12622, Egypt

electron densities around the donor atoms of an inhibitor molecule strongly influence the adsorption and corrosion inhibiting abilities of the inhibitor. Furthermore, steric factors and the type of functional groups present in a compound used as inhibitors are also very important.[12–15]

Acridine derivatives, which are widely used as antibacterial and antiprotozoal agents are the derivatives of tricyclic nitrogen heterocyclic compounds.[16] Acridine derivatives are reported to have unique physical and chemical properties, biological activities, and industrial applications.[17] The use of acridine derivatives as corrosion inhibitors have been reported in literature. The influence of toluidine and acridine derivatives on the corrosion of 63/37 brass in nitric acid solution was reported to be excellent, with efficiency attributed to the elimination of nitrous acid as well as the adsorption of onium type ions at the metal surface.[18] Diffusion and ionization steps associated with the dissolution of α-brass in 1 M NaCl + 0.01 M HCl solution had been found to be inhibited by alkyl acridinium halides. The compounds were also found to be effective in inhibiting copper dissolution than brass.[19]

Following the existing history of corrosion inhibition by acridine derivatives, the present work reports the corrosion inhibition properties of some novel acridine-based thiosemicarbazones namely (2*E*,2′*E*)-2,2′-(3,3,6,6-tetramethyl-9-phenyl-3,4,6,7-tetrahydroacridine-1,8(2*H*,5*H*,9*H*,10*H*)-diylidene)bis(*N*-phenylhydrazinecarbothioamide) (IAB-NP), (2*E*,2′*E*)-2,2′-(3,3,6,6-tetramethyl-9-phenyl-3,4,6,7-tetrahydroacridine-1,8(2*H*,5*H*,9*H*,10*H*)-diylidene)bis(*N*-(2,4-difluorophenyl) hydrazinecarbothioamide) (IAB-ND) and (2*E*,2′*E*)-2,2′-(3,3,6,6-tetramethyl-9-phenyl-3,4,6,7-tetrahydroacridine-1,8(2*H*,5*H*,9*H*,10*H*)-diylidene)bis(*N*-(2-fluorophenyl) hydrazinecarbothioamide) (IAB-NF) for mild steel in 1 M HCl. The effects of IAB-NP, IAB-ND and IAB-NF on mild steel corrosion in the acid were investigated using electrochemical and scanning electron microscopy techniques. Theoretical computational studies were carried out on the novel compounds using density functional theory (DFT) and Monte Carlo simulation calculations. The compounds in this study were synthesized as outlined in Scheme 1.[20] It is anticipated that the presence of functional groups such as –C=C–, –C=N–, –N=N–, –NH, –C=S and π-bonds will enhance the adsorption of the molecules on mild steel surface. The compounds differ in the number of fluorine (F^-) substituents on the phenyl rings, such that IAB-NP is unsubstituted, IAB-NF has one F-substituent at position 2 on the phenyl ring (2-F substituted) and IAB-ND has two F-substituents at positions 2 and 4, *i.e.* it is 2,4-F substituted. The effect of F-substitution on the phenyl ring on corrosion inhibition potentials of the compounds is therefore examined.

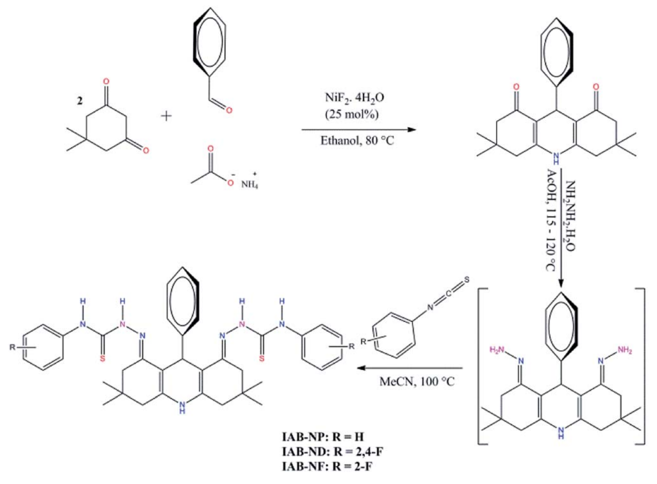

Scheme 1 Synthetic protocol for inhibitors IAB-NP, IAB-ND and IAB-NF.[20]

Experimental and computational studies

Synthesis and characterization of acridine-based thiosemicarbazones IAB-NP, IAB-ND and IAB-NF

The synthesis protocol for inhibitors IAB-NP, IAB-ND and IAB-NF is as outlined in Scheme 1. Detailed procedures, purification methods, experimental yields and spectroscopy data, including proton nuclear magnetic resonance (^1H NMR), carbon-13 nuclear magnetic resonance (^{13}C NMR), Fourier transform infrared spectroscopy (FTIR), electron-spray ionization mass spectroscopy (ESI-MS) and heteronuclear multiple bond correlation HMBC have been reported elsewhere.[20]

Materials

Chemical composition of mild steel samples employed for electrochemical and surface morphology studies was determined prior to use; 0.076% C, 0.039% Ni, 0.015% P, 0.050% Cr, 0.030% S and 99.456% Fe. The samples of steel used for electrochemical measurements were press-cut into 1 cm^2 surface area. Before all measurements and analyses were done, mild steel surface was ground with different grade of emery papers (600, 800 and 1200), washed with double distilled water, degreased with ethanol and acetone and dried at room temperature and used immediately. The corrosive solution, 1 M HCl was prepared by carefully diluting appropriate amount of 32% analytical grade HCl (purchased from Merck South Africa) with double distilled water.

Inhibitor solution

A stock solution of the respective inhibitors (concentration of 0.15 mM) were prepared by first dissolution in 5 mL of acetone (5% equivalent), and subsequently diluted to various concentrations; 0.13, 0.09, 0.07 and 0.05 mM.

Electrochemical measurements

The working electrode employed in these measurements was a mild steel coupon with exposed area of 1 cm^2. The other components of the electrochemical cell include Ag/AgCl (3 M KCl) as the reference electrode and a platinum rod as the counter electrode. All measurements were carried out at 25 ± 1 °C on Metrohm AutoLab Potentiostat/Galvanostat (PGSTAT302N) driven by AutoLab Nova 2.1 software. To ensure a stable open circuit potential (OCP), the working electrode was immersed in the test solution for 30 min during which it undergoes free corrosion in the electrolyte before each measurement.[21]

The mild steel working electrode potential in the corrosive electrolyte was swept between −250 mV and +250 mV relative to the OCP at a scan rate of 1 mV s^{-1}. By extrapolating the linear regions of the polarization curves, electrochemical parameters like corrosion potential (E_{corr}), corrosion current density (i_{corr}), anodic Tafel slope (β_a) and cathodic Tafel slope (β_c) were obtained and recorded. From the derived corrosion densities, the protection abilities were calculated using eqn (1):

$$\%\ \mathrm{IE_{PDP}} = \frac{i^{o}_{corr} - i^{i}_{corr}}{i^{o}_{corr}} \times 100 \tag{1}$$

where i^{i}_{corr} and i^{o}_{corr} represents the corrosion current densities for inhibited and uninhibited systems, respectively, and % $\mathrm{IE_{PDP}}$ is the percentage inhibition efficiency.

An alternating current signal of 10 mV was allowed to pass through the electrochemical unit at a range of 10^{-1} Hz to 105 Hz frequency (at OCP) to record electrochemical impedance spectroscopy (EIS). The EIS spectra were fitted into a suitable Randle's equivalent circuit and relevant parameters were recorded including the charge transfer resistance. The percentage inhibition efficiency (% $\mathrm{IE_{EIS}}$) was calculated using eqn (2):

$$\%\ \mathrm{IE_{EIS}} = \frac{R_{ct} - R^{o}_{ct}}{R_{ct}} \times 100 \tag{2}$$

where R^{o}_{ct} and R_{ct} are the charge transfer resistance without the inhibitors and in the presence of the inhibitors, respectively. For more accuracy and reproducibility of experimental data, the electrochemical studies were performed triply at each tested concentration of the tested inhibitors and mean values are reported.

Surface morphology studies

Scanning electron microscope (SEM) model JEOL JSM-6610 LV was used for surface analysis of the mild steel coupon (1 cm^2) allowed to corrode without and in the presence of optimum concentration of IAB-NF for 24 h.[22] The coupon was removed from the corrosive solution after 24 h, gently washed with double distilled water, acetone and air dried before analysis.

Quantum chemical calculations details

The studied inhibitor molecules were subjected to quantum chemical calculations using the density functional theory (DFT) with the Becke-3-parameter (hybrid) combined with Lee–Yang–Parr (correlation) functionals (B3LYP) and 6-31G basis set.[23–25] The calculations were performed with Gaussian 09.[26] The initial and optimized structures of the molecules and their frontier molecular orbital iso-surfaces observed with the aid of GaussView 5.0. Frontier molecular orbital energy parameters, that is, energy of the highest occupied molecular orbital (E_{HOMO}) and energy of the lowest unoccupied molecular orbital (E_{LUMO}) were derived for the most stable configurations of the molecules. Global electronegativity (χ) and fraction of electron transferred (ΔN) from inhibitor molecule to the metal were calculated according to the equations:[27]

$$\chi = -\frac{1}{2}(E_{\mathrm{LUMO}} - E_{\mathrm{HOMO}}) \tag{3}$$

$$\Delta N = \frac{\varphi_{\mathrm{Fe}} - \chi_{\mathrm{inh}}}{2(\eta_{\mathrm{Fe}} + \eta_{\mathrm{inh}})} \tag{4}$$

where χ_{inh} and η_{inh} are the electronegativity and hardness of the inhibitor respectively, $\varphi_{\mathrm{Fe(110)}}$ is the work function of the body-centered cubic (bcc) crystal structure of Fe(110), and η_{Fe} is the hardness of Fe. The parameter, $\varphi_{\mathrm{Fe(110)}}$ has been reported to have a value of 4.82 eV (ref. 28) and has been successfully used in literature[27,29] while was taken to be 0 eV mol^{-1}.[30] The work function, φ is a better descriptor of charge density of metal than electronegativity.[29]

Monte Carlo simulations details

The adsorption of isolated molecules of IAB-NP, IAB-ND and IAB-NF on Fe(110) surface and their competitive adsorption in the presence of water molecules on the same crystal surface were investigated using the Monte Carlo simulation approach. Fe(110) was used as a representative crystal surface for mild steel, being essentially Fe. Moreover, Fe(110) cleaved plane is a more appropriate surface than Fe(100) and Fe(111) based on its favourable energetics and atomic density and this informed its adoption in this study.[31,32] The DFT optimized structures of the inhibitor molecules were imported into the Materials Studio 6.0 and subjected to another geometry optimization with Forcite calculations for further energy refinement using the Conjugate Gradient algorithm at convergence tolerance 2 × 10^{-5} kcal mol^{-1} (for the energy), 0.001 kcal mol^{-1} Å^{-1} (for the force), 10^{-5} Å (for the displacement), and maximum of 500 iteration. H_2O molecule was optimized at the same level of theory. Fe crystal was imported from Materials Studio library, cleaved into (110) plane, optimized using the Forcite module with Universal Force Field before enlarged into a 10 × 10 super cell and embedded in a vacuum slab.

An optimized isolated inhibitor molecule was made to interact with the Fe(110) surface at a maximum distance of 15 Å to the surface region of the Fe(110) crystal in a simulated annealing task by invoking the adsorption locator module. The iterative interactions were carried out at ultrafine quality using Smart algorithm and the energy parameters were calculated with condensed-phase optimized molecular potentials for atomistic simulation studies-27 (COMPASS27) force field. Competitive adsorption of the inhibitor molecules in the presence of 100 molecules of H_2O was carried out in a similar approach. The equilibrium configurations of inhibitor/Fe(110) and inhibitor/100 H_2O/Fe(110) were determined for each of IAB-NP, IAB-ND and IAB-NF and their corresponding adsorption energies (E_{ads}) were recorded.

Results and discussion

Potentiodynamic polarization study

A potentiodynamic polarization measurement was carried out for all studied inhibitors at various concentrations (0.05 mM to 0.15 mM). The cathodic and anodic Tafel plots of metal exposed to a corrosive solution (1 M HCl) without the inhibitors and in the presence of various concentrations of IAB-NP, IAB-ND and IAB-NF, respectively are represented in Fig. 1. Table 1 show basic parameters (corrosion potential, E_{corr}, anodic and cathodic Tafel slopes, β_a and β_c and corrosion current density, i_{corr}) which were extracted by extrapolating the linear region of the cathodic and anodic branches of the Tafel curves. Furthermore, percentage of inhibition efficiency (% $\mathrm{IE_{PDP}}$) at each concentration recorded were calculated using eqn (1). Careful observation of Fig. 1 shows that evolution of hydrogen gas was stunted and the anodic dissolution of the mild steel was reduced, suggesting that the studied inhibitors repressed the corrosion of the metal. A prominent suppression was obtained in the cathodic branches of the inhibited Tafel plots compared to that of the blank at all concentrations, suggesting the inhibitors could be acting as cathodic inhibitors.[33]

However, Table 1 shows that the changes in E_{corr} did not follow any particular pattern, and there was no significant change in E_{corr} of the inhibited system compared to that recorded for the reaction without the inhibitors. The pattern obtained for E_{corr} in this study suggests that the mechanism of corrosion did not change both in the inhibited and uninhibited systems and shows that the studied compounds behaved as mixed-type inhibitors.[34,35] Generally, there is a shift towards lower current densities for both the anodic and cathodic branches of the Tafel plots (Fig. 1) in the presence of the studied inhibitors compared to the blank. The anodic branch of Tafel plots similar to what we obtained in this study has been attributed to possible formation of nonpassive film *via* the deposition of impurities or small quantity of the products of corrosion on the surface of the metal.[36,37] Increase in concentration of all studied inhibitors resulted in higher polarization, showing a better inhibition efficiency. Thus, the order of inhibition efficiency of the tested corrosion inhibitors at the optimum concentration of 0.15 mM follows: IAB-NF (90.89%) > IAB-ND (85.59%) > IAB-NP (81.13%).

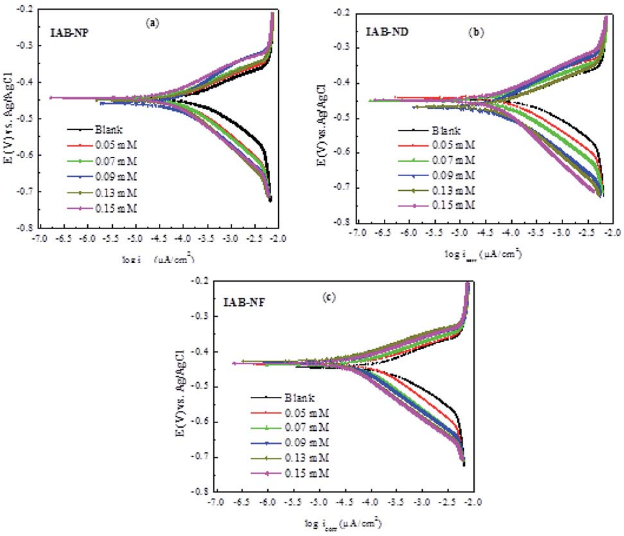

Fig. 1 (a–c) Tafel polarization plots for mild steel corrosion in the absence and presence of various concentrations of IAB-NP, IAB-ND and IAB-NF.

Electrochemical impedance spectroscopy

To gain more insights into the surface properties of the corroding mild steel and the inhibitor as well as to monitor the corrosion of mild steel against time, EIS measurements were carried out. Table 2 contains electrochemical impedance parameters, including solution resistance (R_s), charge transfer resistance (R_p), phase shift (n), double layer capacitance (C_{dl}), and the inhibition efficiencies (% $\mathrm{EI_{EIS}}$) (calculated according to eqn (2)).

The Nyquist plots and Bode diagrams of mild steel in 1.0 M HCl without the inhibitors and with the addition of varying concentrations of IAB-NP, IAB-ND and IAB-NF are represented in Fig. 2 and 3, respectively. As observed in the Nyquist plots, single depressed semicircle with its centre under the real axis indicates that the dissolution of mild steel and hydrogen evolution in the studied corrosive electrolyte features single charge transfer process.[38] Larger diameter of semicircles associated with inhibitor containing solutions in comparison to the blank is an indication of possible formation of adsorbed film of the inhibitor molecules on the metal surface.[39] The corrosion mechanism of mild steel in 1 M HCl was not altered by the addition of the inhibitor molecules as revealed by the similar shape of the Nyquist plots in the absence and presence of the inhibitors.[40] The order of R_p values is inversely proportional to the protection efficiencies of the inhibitors.[41,42]

The phase angle modulation with frequency and impedance for corrosion of mild steel in 1 M HCl without the inhibitors and in the presence of the respective inhibitors is represented by the Bode plots (Fig. 3). Bode plots provides vital information about the inductive, capacitive and resistive behaviours of the system at different frequencies. The impedance spectra were analysed using the electrical equivalent circuit represented in Fig. 4, and a perfect fit for experimental data was obtained and recorded in Table 2. The pure double-layer capacitor (C_{dl}) was replaced in the Randle's equivalent circuit with the constant phase element (CPE) to ensure a more accurate fit. Eqn (5) was employed in the calculations of C_{dl} using the values of n and Y_0, where the magnitude of CPE and derivation parameters ($-1 \leq n \leq 1$) depends on the surface morphology;[43,44]

$$C_{\mathrm{dl}} = \left(Y_{\mathrm{o}} R_{\mathrm{p}}^{1-n}\right)^{1/n} \tag{5}$$

were n represents the CPE exponent and Y_{o} is the CPE constant, respectively.

At intermediate frequencies, an increase in slope for all studied inhibitors with increasing concentrations is observed when looking at the linear portion of the Bode impedance modulus plots (Fig. 3). This is a strong indication that inhibitor molecules modify the surface of the mild steel as well as changing the electrochemistry of the surface.[22] The values of n (CPE exponent) is linked to the nature of the interface between the adsorbed inhibitors on the mild steel (which enables protection from corrosion) and the corrosive media.[45] The values of n in this study (Table 2) are very close to unity, and

Table 1 Electrochemical parameters (±SD) and inhibition efficiencies obtained from potentiodynamic polarization measurements

Inhibitor	Conc. (mM)	$-E_{corr}$ (mV)	β_a (mV dec^{-1})	β_c (mV dec^{-1})	i_{corr} (μA cm^{-2})	% IE$_{PDP}$
Blank	1.0	445.48	111.22 (±1.02)	116.28 (±1.12)	317.65 (±1.87)	—
IAB-NP	0.05	448.25	110.16 (±1.12)	75.41 (±1.34)	128.84 (±1.35)	59.44
	0.07	444.06	109.79 (±1.05)	77.37 (±1.22)	104.43 (±1.04)	67.12
	0.09	457.71	112.54 (±1.34)	108.44 (±1.46)	95.06 (±1.24)	70.07
	0.13	449.20	119.54 (±1.26)	64.86 (±1.05)	81.80 (±0.95)	74.25
	0.15	443.37	109.32 (±1.12)	79.44 (±0.98)	59.95 (±1.53)	81.13
IAB-ND	0.05	440.70	98.83 (±0.85)	88.40 (±1.24)	108.88 (±1.44)	65.72
	0.07	449.41	107.15 (±1.34)	93.74 (±1.76)	92.58 (±1.36)	70.85
	0.09	467.16	112.46 (±1.26)	120.13 (±1.65)	69.93 (±0.25)	77.99
	0.13	464.65	118.35 (±1.15)	63.88 (±1.15)	61.45 (±1.53)	80.65
	0.15	447.79	135.11 (±1.42)	75.14 (±0.75)	45.77 (±1.12)	85.59
IAB-NF	0.05	436.95	111.51 (±1.45)	55.40 (±1.32)	136.20 (±1.65)	57.12
	0.07	437.83	106.75 (±0.98)	50.71 (±1.25)	61.02 (±0.98)	80.79
	0.09	430.80	104.20 (±1.32)	54.83 (±0.95)	46.13 (±1.24)	85.48
	0.13	427.54	104.63 (±1.52)	50.04 (±1.85)	30.09 (±1.21)	90.53
	0.15	433.80	102.85 (±0.75)	47.26 (±0.55)	28.94 (±0.65)	90.89

could be inferred that the interface is pseudo-capacitive in nature. The decrease in the values of C_{dl} in the presence of IAB-NP, IAB-ND and IAB-NF, respectively compared to C_{dl} value for the blank (Table 2) could be attributed to the adsorption of the inhibitor molecules on the surface of the metal, thereby increasing the thickness of the protecting layer at the interface of the corrosive solution and the mild steel.[46,47] The inhibition efficiencies from EIS were consistent with that obtained from PDP studies.

Adsorption isotherms

The experimental data obtained from PDP and EIS analyses were fitted into different adsorption isotherms including Langmuir, Temkin, Freundlich and Frumkin to determine the adsorption mechanism between the molecules of the inhibitors and the adsorption sites on the metal surfaces.[21,35] The linear form of the Langmuir adsorption isotherm (eqn (6))[48] gave better fits with values of regression coefficients (R^2) greater than 0.9 and indicated the possibility of the formation of one monolayer of the inhibitor on the metal surface:[49]

$$\frac{C_{inh}}{\theta} = C_{inh} + \frac{1}{K_{ads}} \tag{6}$$

where K_{ads} represents the equilibrium constant associated with adsorption of the inhibitor on the surface of the metal, θ is the degree of surface coverage and C_{inh} is the inhibitor concentrations. Langmuir plots are presented in Fig. 5 (as obtained from EIS and PDP techniques), and calculated values of K_{ads} are recorded in Table 3. The significant of K_{ads} values are that higher values depict better adsorption of the inhibitor molecules resulting in better protection efficiencies. However, deviation from unity of values for slope as obtained for some experimental methods (Table 3) could be attributed to the

Table 2 EIS parameters (±SD) for corrosion of mild steel in 1.0 M HCl without and with varying concentrations (0.05–0.15 mM) of IAB-NP, IAB-ND and IAB-NF

Inhibitor	Conc. (mM)	R_s (Ω cm^2)	R_p (Ω cm^2)	C_{dl} (μF cm^{-2})	n	% IE$_{EIS}$
Blank	0	1.04 (±0.05)	15.9 (±0.3)	444	0.90	—
IAB-NP	0.05	1.26 (±0.02)	42.6 (±0.4)	289	0.88	62.68
	0.07	1.08 (±0.01)	44.8 (±0.2)	301	0.89	64.51
	0.09	1.16 (±0.02)	50.2 (±0.2)	268	0.89	68.33
	0.13	1.63 (±0.03)	63.8 (±0.1)	252	0.88	75.08
	0.15	1.60 (±0.01)	108.0 (±0.2)	187	0.88	85.28
IAB-ND	0.05	1.08 (±0.02)	32.6 (±0.1)	328	0.89	51.23
	0.07	1.52 (±0.01)	51.1 (±0.1)	251	0.88	68.88
	0.09	1.36 (±0.03)	90.5 (±0.3)	201	0.88	82.43
	0.13	1.21 (±0.03)	94.8 (±0.1)	264	0.88	83.23
	0.15	1.66 (±0.02)	127.0 (±0.2)	105	0.89	87.48
IAB-NF	0.05	1.06 (±0.03)	40.2 (±0.1)	331	0.89	60.45
	0.07	1.23 (±0.03)	84.2 (±0.1)	262	0.88	81.12
	0.09	1.21 (±0.01)	94.8 (±0.3)	264	0.88	83.23
	0.13	1.20 (±0.02)	156.0 (±0.1)	101	0.90	89.81
	0.15	1.35 (±0.02)	167.0 (±0.85)	145	0.88	90.48

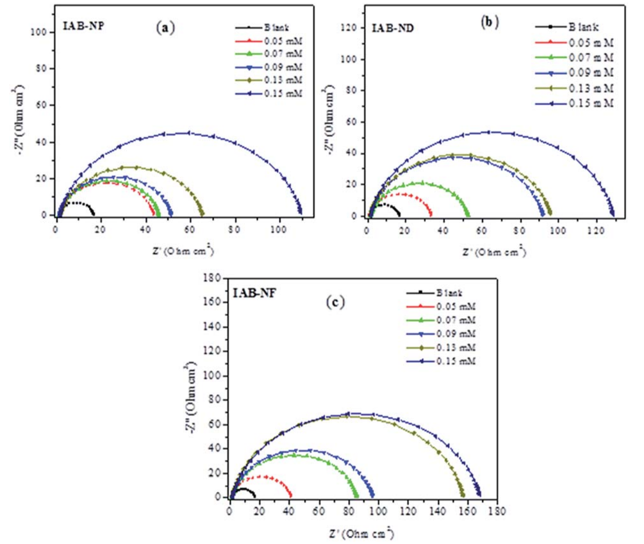

Fig. 2 (a–c) Nyquist plots for mild steel corrosion without the inhibitors and in the presence of various concentrations of IAB-NP, IAB-ND and IAB-NF.

likelihood of large organic molecules attaching to more than one adsorption site on the metal. Similar observations has been reported previously.[50,51]

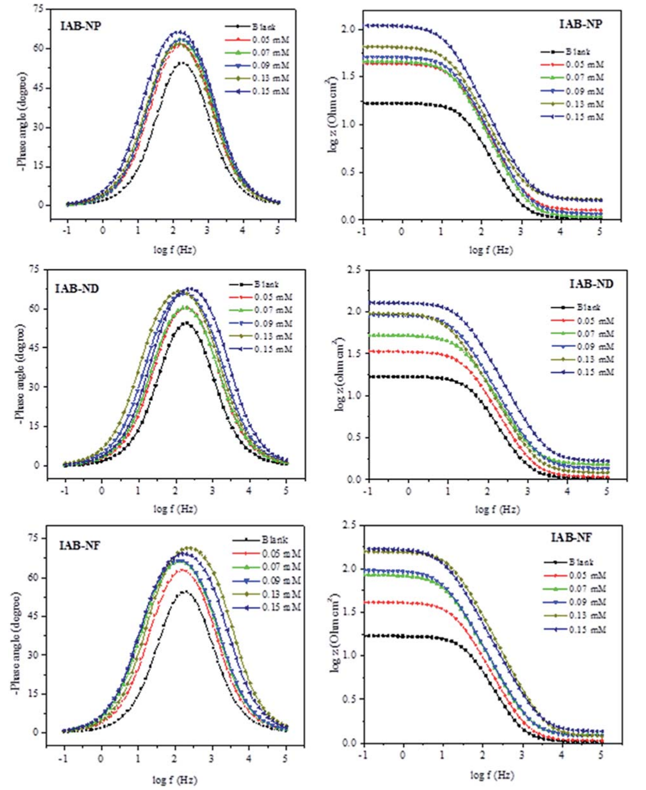

Fig. 3 Bode plots for mild steel corrosion in the absence and presence of various concentrations of IAB-NP, IAB-ND and IAB-NF.

Fig. 4 Randle's equivalent circuit for fitting EIS spectra.

The standard free energies of adsorption ΔG^{o}_{ads} were calculated from eqn (7) using values of K_{ads} obtained from Langmuir isotherm, with R and T having their usual meanings and 55.5 represent the molar concentration of water in solution:[52]

$$\Delta G^{o}_{ads} = -RT\ln(55.5\ K_{ads}) \tag{7}$$

The standard free energy of adsorption enables the deduction of how spontaneous the protection processes are as well as the stability of adsorption on the metal.[53] The values of ΔG^{o}_{ads} ranging between -34.57 to 36.27 kJ mol^{-1} obtained in this study (Table 3) give a strong indication of a combination of two processes; transfer or sharing of electron from or between the inhibitor molecules to the metal surface resulting in the formation a coordinate type bond, as well as an electrostatic interaction between the charged molecules of the inhibitors and the charge surface of the metal. Literature reports classify range of values of ΔG^{o}_{ads} similar to what we obtained in this study for mixed-type adsorption (chemisorption and physisorption).[4,7,43] However, there is stability of the adsorbed layer and spontaneity associated with our inhibitors as indicated by the negative values of ΔG^{o}_{ads}, and the values are closer to -40 kJ mol^{-1} indicating that the processes of adsorption was tending towards chemisorption mechanism.

Surface morphology studies

Mild steel coupons (1 cm^2 surface area) that were immersed in 1 M HCl in the absence and presence of 0.15 mM IAB-NF for

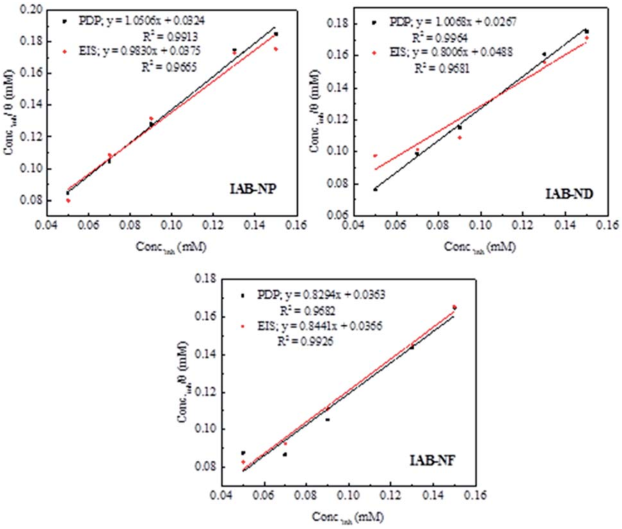

Fig. 5 Langmuir adsorption isotherm for mild steel corrosion in 1.0 M HCl using PDP and EIS methods for various concentrations of IAB-NP, IAB-ND and IAB-NF.

Table 3 Langmuir adsorption isotherm parameters of mild steel corrosion in 1.0 M HCl at 298 K for the utilized inhibitors

Inhibitor	Method	K_{ads} (M^{-1})	$-\Delta G^o_{ads}$ (kJ mol^{-1})	Slope
IAB-NP	PDP	3.09×10^4	35.59	1.051
	EIS	2.67×10^4	35.23	0.983
IAB-ND	PDP	3.76×10^4	36.07	1.007
	EIS	2.05×10^4	34.57	0.801
IAB-NF	PDP	2.75×10^4	35.29	0.829
	EIS	2.73×10^4	35.28	0.844

24 h were subjected to SEM analysis. Surface morphology of mild steel in the presence of inhibitors was only examined for IAB-NF as a representative result since IAB-NF gave the highest inhibition efficiency at 0.15 mM. The SEM micrographs (Fig. 6) gave an indication of protective effects of the inhibitor molecules on mild steel surface. Mild steel surface before immersion (Fig. 6a) exhibits plain surface with minor indention due to abrasion with emery paper. Gross damage depicted on the surface of metal coupon immersed in 1.0 M HCl without the inhibitors is as a result of possible nonstop attack of chloride ions from the acid on the metal. The mild steel retrieved from solution containing 0.15 mM IAB-NF reveals that the surface damage was not pronounced, hence confirming proper surface coverage *via* adsorption and protection by the inhibitors.

DFT study on the inhibitors

Optimized structures, HOMO and LUMO iso-surfaces of the studied compounds are shown in Fig. 7. The three compounds showed similar electron density distributions of HOMO and LUMO. The HOMO electron density is distributed over the two symmetric phenylhydrazine moieties of the molecules. In all the three molecules, the 9-phenylacridine moiety does not contribute to the HOMO. For the studied molecules to adsorb on the metal, charge donation from the inhibitor molecules to the vacant orbitals of the metals will occur essentially through the phenylhydrazine moieties. For both IAB-ND and IAB-NF which contain two and one fluorine atom(s) respectively, the fluorine atoms are also involved in the HOMO. The LUMO electron density of the molecules, like the HOMO is also distributed over the phenylhydrazine moieties. However, unlike the HOMO, the pyridine ring of the acridine is also involved in the LUMO, suggesting that possible back-donation from

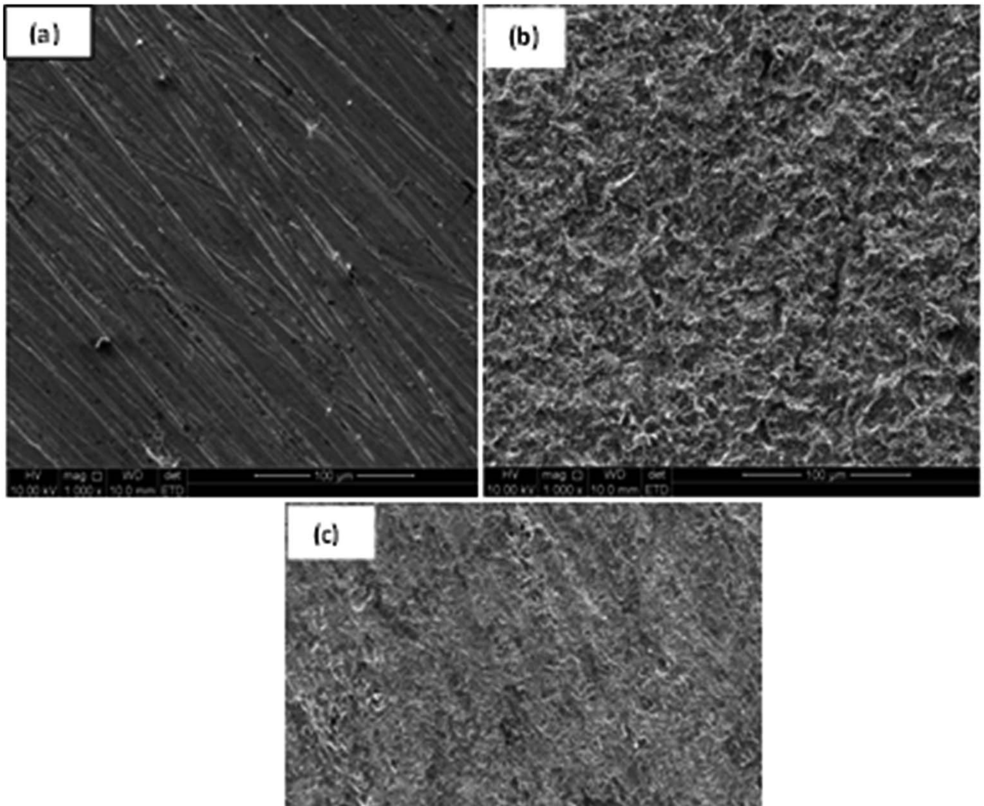

Fig. 6 (a–c) SEM micrographs of surfaces of mild steel: (a) abraded, (b) in 1.0 M HCl, (c) in the presence of 0.15 M of IAB-NF.

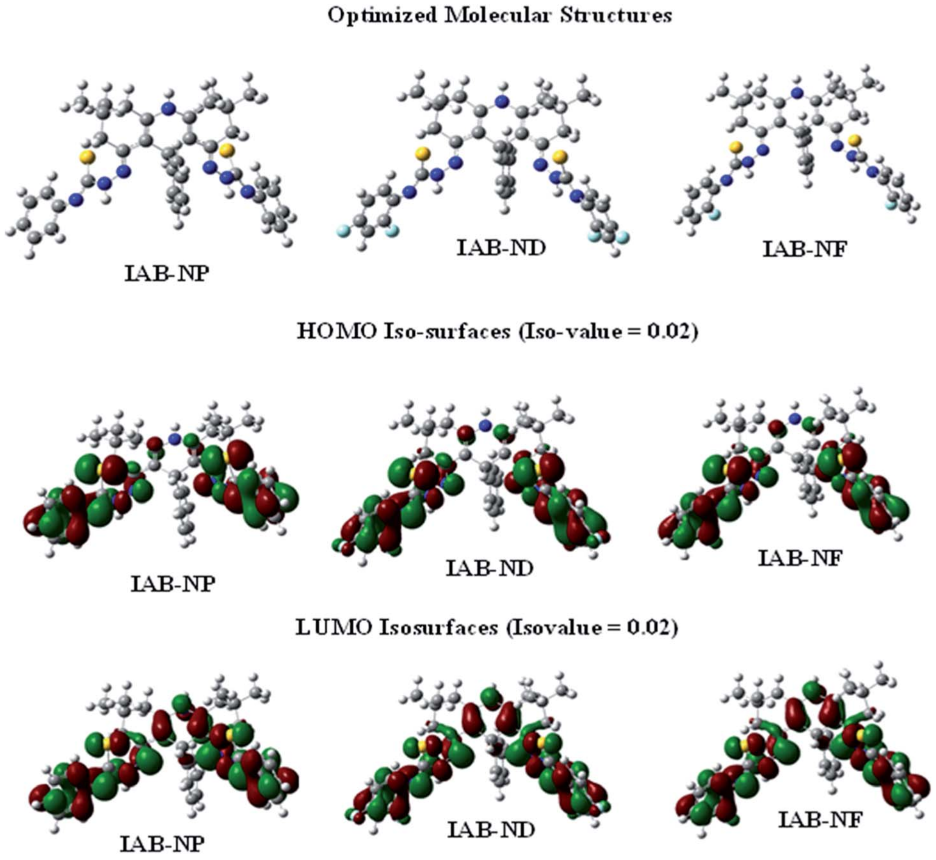

Fig. 7 Optimized structures, HOMO and LUMO iso-surfaces of the studied compounds.

occupied orbitals of the metal to the inhibitors will involve the acridine ring.

Gas and aqueous phases quantum chemical reactivity indices of the molecules are listed in Table 4. There is no simple direct correlation between the inhibitive potentials of the molecules and their calculated reactivity indices. However, both IAB-ND and IAB-NF with lower E_{LUMO} and ΔE (in aqueous phase) compared to IAB-NP showed higher inhibition efficiencies. IAB-ND and IAB-NF also showed higher electronegativity (χ) and lower fraction of electron donation (ΔN) than IAB-NP. These observations suggest that IAB-ND and IAB-NF are more disposed to back-donation than IAB-NP and this might promote the adsorption of IAB-ND and IAB-NF molecules onto mild steel surface better than IAB-NP. This might in turn inform higher corrosion inhibition potentials of IAB-ND and IAB-NF compared to IAB-NP. The relatively high inhibition potentials of IAB-ND and IAB-NF might also be related to favourable dipole–dipole interactions between their molecules and polarized steel surface due to high dipole moments of the inhibitor molecules. IAB-NP with the least inhibition efficiency also has the least dipole moment.

Monte Carlo simulations

The interactions between inhibitor molecules and mild steel were theoretically modelled using the Monte Carlo simulations while the mild steel was represented by a cleaved Fe(110)

Table 4 Reactivity indices for the inhibitors

Inhibitors	E_{HOMO} (eV)	E_{LUMO} (eV)	ΔE (eV)	χ (eV)	ΔN	Dipole moment
Gas phase						
IAB-NP	−4.748	−4.313	0.435	4.531	0.665	7.371
IAB-ND	−5.023	−4.556	0.467	4.790	0.065	11.194
IAB-NF	−4.879	−4.417	0.462	4.648	0.373	7.778
Aqueous phase						
IAB-NP	−5.437	−4.512	0.925	4.975	−0.167	16.165
IAB-ND	−5.445	−4.762	0.683	5.103	−0.414	22.851
IAB-NF	−5.459	−4.757	0.702	5.108	−0.411	21.042

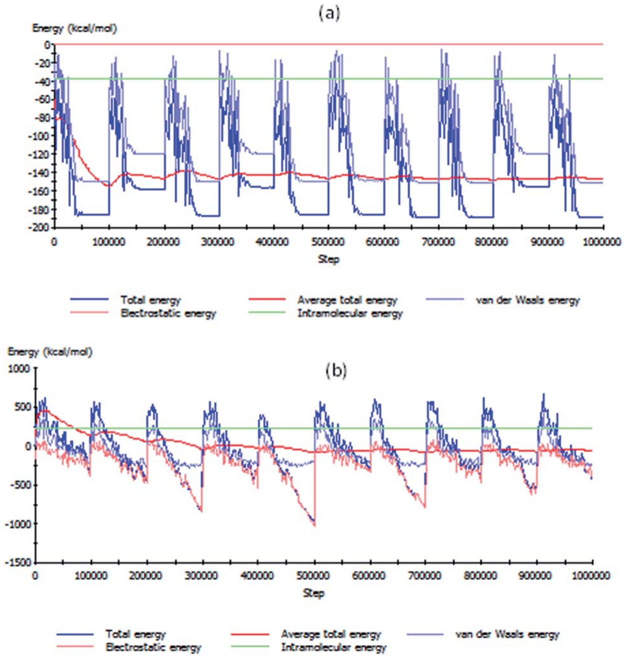

Fig. 8 Variation of energy terms with optimization steps for the adsorption systems (a) IAB-NP/Fe(110) and (b) IAB-NP + 100 H_2O/Fe(110).

surface. The simulation was carried out both in the absence and presence of water molecules. The representative profiles for the variation of various energy terms involved in the interaction with optimization step are shown in Fig. 8. The energy profiles in Fig. 8 revealed that optimization of major energy components was achieved within the adopted number of optimization steps. The adsorption of inhibitor molecules on Fe(110) is depicted by the images in Fig. 9 both in the absence and presence of 100 molecules of H_2O. The results showed that the inhibitor molecules have the tendency of displacing H_2O molecules from their adsorption sites and consequently adsorb on the Fe surface. The orientation of the inhibitor molecules on Fe(110) surface appears to depend on the resulting interactions between the particular inhibitor molecules and the neighbouring H_2O molecules. The values of the adsorption energy (E_{ads}) showed that IAB-NF and IAB-ND have higher adsorption capacities than IAB-NP, which is in agreement with what was observed experimentally and corroborated by DFT study.

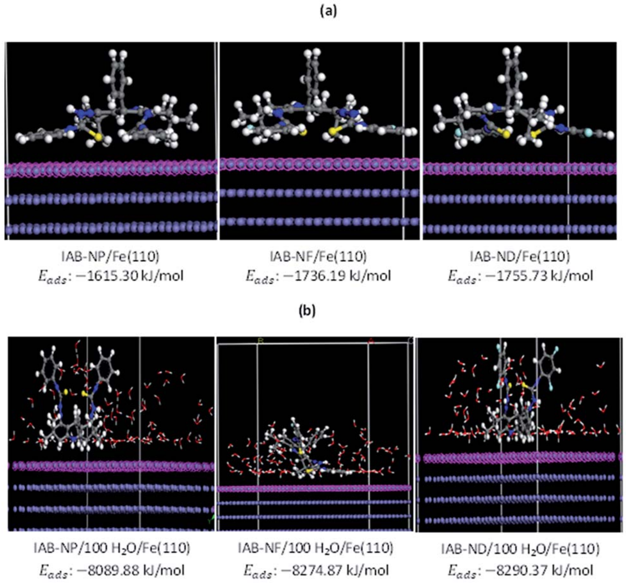

IAB-NP/Fe(110) E_{ads}: −1615.30 kJ/mol
IAB-NF/Fe(110) E_{ads}: −1736.19 kJ/mol
IAB-ND/Fe(110) E_{ads}: −1755.73 kJ/mol

IAB-NP/100 H_2O/Fe(110) E_{ads}: −8089.88 kJ/mol
IAB-NF/100 H_2O/Fe(110) E_{ads}: −8274.87 kJ/mol
IAB-ND/100 H_2O/Fe(110) E_{ads}: −8290.37 kJ/mol

Fig. 9 Equilibrium Monte Carlo configurations of (a) IAB-NP/Fe(110), IAB-NF/Fe(110) and IAB-ND/Fe(110) and (b) IAB-NP + 100 H_2O/Fe(110), IAB-NF + 100 H_2O/Fe(110) and IAB-ND + 100 H_2O/Fe(110).

Conclusions

The effects of some acridine-based thiosemicarbazones on the corrosion of mild steel in 1 M HCl solution were investigated using electrochemical measurements, surface morphology analyses and theoretical calculations. Based on the results obtained and presented, it can be concluded that:

(1) The acridine-based thiosemicarbazones (IAB-NP, IAB-ND and IAB-NF) acted as excellent inhibitors for the corrosion of mild steel, with order of inhibition efficiency: IAB-NF > IAB-ND > IAB-NP.

(2) Tafel polarization results revealed that the investigated inhibitors behaved as mixed-type corrosion inhibitors.

(3) The studied inhibitors obeyed the Langmuir adsorption isotherm, and standard free energies of adsorption suggested chemisorption and physisorption mechanisms.

(4) SEM analyses show that the inhibitors protect the mild steel from electrolyte ions attacks by the formation of protective film at the metal surface.

(5) DFT study suggested that IAB-ND and IAB-NF have higher tendency for back-bonding with the metal than IAB-NP and this enhanced their inhibition efficiency.

(6) Monte Carlo simulations revealed that the adsorption of IAB-ND and IAB-NF molecules on Fe(110) surface is stronger and more favourable than that of IAB-NP.

Conflicts of interest

There are no conflicts to declare.

Acknowledgements

E. D. Akpan and L. O. Olasunkanmi acknowledge the North-West University (Mafikeng campus), South Africa for providing financial assistance under the Postdoctoral Fellowship Scheme. The authors would like to extend their sincere appreciation to the Researchers Supporting Project number (RSP-2019/33), King Saud University, Riyadh. Authors acknowledge the Centre for High Performance and Computing (CHPC), CSIR, South Africa for granting access to the computing resources.

References

1 N. R. Baddoo, *J. Constr. Steel Res.*, 2008, **64**, 1199–1206.

2 X.-q. Hu, C.-h. Liang and N.-b. Huang, *J. Iron Steel Res. Int.*, 2006, **13**, 56–60.

3 N. S. Ayati, S. Khandandel, M. Momeni, M. H. Moayed, A. Davoodi and M. Rahimizadeh, *Mater. Chem. Phys.*, 2011, **126**, 873–879.

4 M. A. Quraishi and J. Rawat, *Corros. Rev.*, 2001, **19**, 273.

5 M. A. Ameer and A. M. Fekry, *Prog. Org. Coat.*, 2011, **71**, 343–349.

6 J. Fu, H. Zang, Y. Wang, S. Li, T. Chen and X. Liu, *Ind. Eng. Chem. Res.*, 2012, **51**, 6377–6386.

7 P. B. Raja, M. Ismail, S. Ghoreishiamiri, J. Mirza, M. C. Ismail, S. Kakooei and A. A. Rahim, *Chem. Eng. Commun.*, 2016, **203**, 1145–1156.

8 P. B. Raja and M. G. Sethuraman, *Mater. Lett.*, 2008, **62**, 113–116.

9 N. A. Negm, F. M. Ghuiba and S. M. Tawfik, *Corros. Sci.*, 2011, **53**, 3566–3575.

10 M. Finšgar and I. Milošev, *Corros. Sci.*, 2010, **52**, 2737–2749.

11 N. Lin, S. Stepanow, F. Vidal, K. Kern, M. S. Alam, S. Stromsdorfer, V. Dremov, P. Muller, A. Landa and M. Ruben, *Dalton Trans.*, 2006, 2794–2800, DOI: 10.1039/b515728e.

12 S. Hettiarachchi, Y. W. Chan, R. B. Wilson and V. S. Agarwala, *MRS Proceedings*, 1988, **125**, 321.

13 A. Singh, Y. Lin, M. Quraishi, L. Olasunkanmi, O. Fayemi, Y. Sasikumar, B. Ramaganthan, I. Bahadur, I. Obot, A. Adekunle, M. Kabanda and E. Ebenso, *Molecules*, 2015, **20**, 15122.

14 M. Dibetsoe, L. Olasunkanmi, O. Fayemi, S. Yesudass, B. Ramaganthan, I. Bahadur, A. Adekunle, M. Kabanda and E. Ebenso, *Molecules*, 2015, **20**, 15701.

15 T. Peme, L. O. Olasunkanmi, I. Bahadur, A. S. Adekunle, M. M. Kabanda and E. E. Ebenso, *Molecules*, 2015, **20**, 16004–16029.

16 A. D. William, *Curr. Med. Chem.*, 2002, **9**, 1655–1665.

17 M. Gensicka-Kowalewska, G. Cholewinski and K. Dzierzbicka, *RSC Adv.*, 2017, **7**, 15776–15804.

18 N. K. Patel and B. B. Patel, *Mater. Corros.*, 1975, **26**, 126–127.

19 V. V. Ekilik, M. N. Svyataya and A. G. Berezhnaya, *Russ. J. Electrochem.*, 2003, **39**, 857–862.

20 I. O. Isaac, I. Munir, M. al-Rashida, S. A. Ali, Z. Shafiq, M. Islam, R. Ludwig, K. Ayub, K. M. Khan and A. Hameed, *R. Soc. Open Sci.*, 2018, **5**, 180646.

21 L. C. Murulana, M. M. Kabanda and E. E. Ebenso, *RSC Adv.*, 2015, **5**, 28743–28761.

22 L. O. Olasunkanmi, M. F. Sebona and E. E. Ebenso, *J. Mol. Struct.*, 2017, **1149**, 549–559.

23 A. D. Becke, *Phys. Rev.*, 1988, **38**, 3098–3100.

24 A. D. Becke, *J. Chem. Phys.*, 1993, **98**, 5648–5652.

25 C. Lee, W. Yang and R. G. Parr, *Phys. Rev. B: Condens. Matter Mater. Phys.*, 1988, **37**, 785–789.

26 M. J. Frisch, G. W. Trucks, H. B. Schlegel, G. E. Scuseria, M. A. Robb, J. R. Cheeseman, G. Scalmani, V. Barone, B. Mennucci, G. A. Petersson, H. Nakatsuji, M. Caricato, X. Li, H. P. Hratchian, A. F. Izmaylov, J. Bloino, G. Zheng, J. L. Sonnenberg, M. Hada, M. Ehara, K. Toyota, R. Fukuda, J. Hasegawa, M. Ishida, T. Nakajima, Y. Honda, O. Kitao, H. Nakai, T. Vreven and J. A. Montgomery, *Gaussian 09 series programs–Revision D.01*, Gaussian, Inc, Wallingford, CT, USA, 2009.

27 M. El Faydy, R. Touir, M. Ebn Touhami, A. Zarrouk, C. Jama, B. Lakhrissi, L. O. Olasunkanmi, E. E. Ebenso and F. Bentiss, *Phys. Chem. Chem. Phys.*, 2018, **20**, 20167–20187.

28 H. Lgaz, R. Salghi and H. I. Ali, *Int. J. Electrochem. Sci.*, 2018, **13**, 250.

29 A. Kokalj, *Chem. Phys.*, 2012, **393**, 1–12.

30 R. G. Pearson, *Inorg. Chem.*, 1988, **27**, 734–740.

31 L. Guo, C. Qi, X. Zheng, R. Zhang, X. Shen and S. Kaya, *RSC Adv.*, 2017, **7**, 29042–29050.

32 L. Xu, D. Kirvassilis, Y. Bai and M. Mavrikakis, *Surf. Sci.*, 2018, **667**, 54–65.

33 K. Marušić, H. O. Ćurković and H. Takenouti, *Electrochim. Acta*, 2011, **56**, 7491–7502.

34 S. Issaadi, T. Douadi, A. Zouaoui, S. Chafaa, M. A. Khan and G. Bouet, *Corros. Sci.*, 2011, **53**, 1484–1488.

35 L. O. Olasunkanmi, I. B. Obot, M. M. Kabanda and E. E. Ebenso, *J. Phys. Chem. C*, 2015, **119**, 16004–16019.

36 L. Toukal, S. Keraghel, F. Benghanem and A. Ourari, *Int. J. Electrochem. Sci.*, 2018, **13**, 951–974.

37 M. A. Deyab, R. Slota, E. Bloise and G. Mele, *RSC Adv.*, 2018, **8**, 1909–1916.

38 I. V. Aoki, I. C. Guedes and S. L. A. Maranhão, *J. Appl. Electrochem.*, 2002, **32**, 915–919.

39 A. Singh, Y. Lin, I. B. Obot and E. E. Ebenso, *J. Mol. Liq.*, 2016, **219**, 865–874.

40 S. K. Shukla and M. A. Quraishi, *Corros. Sci.*, 2009, 51.

41 M. Davoodi and M. Nasr-Esfahani, *Prot. Met. Phys. Chem. Surf.*, 2016, **52**, 149–155.

42 P. M. Dasami, K. Parameswari and S. Chitra, *Orient. J. Chem.*, 2015, **31**, 185–191.

43 C. Verma, L. O. Olasunkanmi, T. W. Quadri, E.-S. M. Sherif and E. E. Ebenso, *J. Phys. Chem. C*, 2018, **122**, 11870–11882.

44 C. Verma, L. O. Olasunkanmi, E. E. Ebenso, M. A. Quraishi and I. B. Obot, *J. Phys. Chem. C*, 2016, **120**, 11598–11611.

45 D. K. Yadav, M. A. Quraishi and B. Maiti, *Corros. Sci.*, 2012, **55**, 254–266.

46 K. R. Ansari and M. A. Quraishi, *Phys. E*, 2015, **69**, 322–331.

47 M. Moradi, J. Duan and X. Du, *Corros. Sci.*, 2013, **69**, 338–345.

48 L. C. Murulana, A. K. Singh, S. K. Shukla, M. M. Kabanda and E. E. Ebenso, *Ind. Eng. Chem. Res.*, 2012, **51**, 13282–13299.

49 D. Zhang, Y. Tang, S. Qi, D. Dong, H. Cang and G. Lu, *Corros. Sci.*, 2016, **102**, 517–522.

50 T. W. Quadri, L. O. Olasunkanmi, O. E. Fayemi, M. M. Solomon and E. E. Ebenso, *ACS Omega*, 2017, **2**, 8421–8437.

51 M. M. Solomon, S. A. Umoren, I. I. Udosoro and A. P. Udoh, *Corros. Sci.*, 2010, **52**, 1317–1325.

52 P. Roy, A. Pal and D. Sukul, *RSC Adv.*, 2014, **4**, 10607–10613.

53 L. C. Murulana, M. M. Kabanda and E. E. Ebenso, *J. Mol. Liq.*, 2016, **215**, 763–779.